Capillary RheoSANS: Measuring the rheology and nanostructure of complex fluids at high shear rates

Journal:	*Soft Matter*
Manuscript ID	SM-ART-05-2020-000941.R1
Article Type:	Paper
Date Submitted by the Author:	17-Jun-2020
Complete List of Authors:	Murphy, Ryan; National Institute of Standards and Technology, NCNR Riedel, Zachary; National Institute of Standards and Technology, NCNR Nakatani, Marshall; National Institute of Standards and Technology, NCNR Salipante, Paul; NIST Material Measurement Laboratory, Polymers and Complex Fluids Group Weston, Javen; Georgetown University, Physics; National Institute of Standards and Technology, Materials Science and Engineering Division Hudson, Steven; NIST, Polymers Division Weigandt, Katie; National Institute of Standards and Technology, NCNR

Soft Matter

ARTICLE TYPE

Cite this: DOI: 00.0000/xxxxxxxxxx

Capillary RheoSANS: Measuring the rheology and nanostructure of complex fluids at high shear rates[†]

Ryan P. Murphy,[a,*] Zachary W. Riedel,[a] Marshall A. Nakatani,[a] Paul F. Salipante,[b] Javen S. Weston,[c] Steven D. Hudson,[b] and Katie M. Weigandt.[a,*]

Received Date
Accepted Date

DOI: 00.0000/xxxxxxxxxx

Complex fluids containing micelles, proteins, polymers and inorganic nanoparticles are often processed and used in high shear environments that can lead to structural changes at the nanoscale. Here, capillary rheometry is combined with small-angle neutron scattering (SANS) to simultaneously measure the viscosity and nanostructure of model complex fluids at industrially-relevant high shear rates. Capillary RheoSANS (CRSANS) uses pressure-driven flow through a long, flexible, silica capillary to generate wall shear rates up to 10^6 s^{-1} and measure pressure drops up to 500 bar. Sample volumes as small as 2 mL are required, which allow for measurement of supply-limited biological and deuterated materials. The device design, rheology and scattering methodologies, and broad sample capabilities are demonstrated by measuring a variety of model systems including silica nanoparticles, NIST monoclonal antibodies, and surfactant worm-like micelles. For a shear-thinning suspension of worm-like micelles, CRSANS measurements are in good agreement with traditional RheoSANS measurements. Collectively, these techniques provide insight into relationships between nanostructure and steady-shear viscosity over eight orders of magnitude in shear rate. Overall, CRSANS expands the capabilities of traditional RheoSANS instruments toward higher shear rates, enabling *in situ* structural measurements of soft materials at shear rates relevant to extrusion, coating, lubrication, and spraying applications.

1 Introduction

The underlying structure of complex fluids can produce non-linear rheological responses under processing conditions such as extrusion, coating, spraying, or lubrication. Many of these applications involve large fluid velocities in confined geometries, and thereby generate large shear rates and shear stresses near the confining wall. Complex fluids containing self-assembled micelles, proteins, polymers, or inorganic nanoparticles can undergo reversible or irreversible structural changes at high shear rates and shear stresses. Depending on the application, these changes may be desired or alternatively lead to degradation of the product.

Various instruments have been developed to measure the nanostructure and rheological properties of complex fluids under different flow conditions.[1–9] In traditional Rheo-small-angle scattering instruments, commercially available rheometers with rotating concentric cylinder geometries are combined with small-angle neutron scattering (SANS), X-ray scattering (SAXS), or light scattering (SALS) to simultaneously measure the sample rheology and microstructure at a single shear rate within the narrow gap.[3,7,10] These methods typically generate shear rates ($\dot{\gamma}$) from $\dot{\gamma} \approx 10^{-3}$ s^{-1} up to maximum shear rates of $\dot{\gamma} \approx 10^3$ s^{-1}. More recently, a μRheoSANS instrument combined SANS and pressure-driven flow within a thin, rectangular slit geometry to produce higher shear rates.[5] The μRheoSANS device measures sample viscosity at wall shear rates up to $\dot{\gamma}_w \approx 10^5$ s^{-1} and with simultaneous SANS measurements up to $\dot{\gamma}_w \approx 10^4$ s^{-1}.[5] To our knowledge, there are no instruments capable of measuring the rheology and nanostructure of complex fluids at shear rates up to 10^6 s^{-1}.

SANS techniques provide a non-destructive, *in situ* method to measure the ensemble-averaged structure of complex fluids in motion.[3,4,6,7,11–16] The scattered intensity $I(q)$ is measured as a function of the scattering wavevector q and provides time-averaged structural information on length scales from approximately 1 nm to 100 nm. In particular, neutron scattering methods can probe the structure of multicomponent mixtures by performing hydrogen-deuterium substitution to adjust the scattering length density contrast between the sample and solvent.

---

[a] *NIST Center for Neutron Research, National Institute of Standards and Technology, 100 Bureau Dr., Gaithersburg, MD, USA. Tel:+1 301 975 8544*

[b] *Materials Science and Engineering Division, National Institute of Standards and Technology, Gaithersburg, MD, USA.*

[c] *Russell School of Chemical Engineering, University of Tulsa, Tulsa, OK, USA.*

∗ *Corresponding authors: ryan.murphy@nist.gov, katie.weigandt@nist.gov*

[†] Electronic Supplementary Information (ESI) available: Experimental setup, protocols, calibrations, sample preparation, and various corrections for capillary rheometry. See DOI: 10.1039/cXsm00000x/

This work presents a capillary rheometer instrument suitable for SANS measurements, termed Capillary RheoSANS (CRSANS), which enables simultaneous measurement of rheology and nanostructure of complex fluids up to shear rates of 10^6 s^{-1}. We first discuss the device setup, measurement methods, and adjustable capillary configurations to optimize the shear rates and scattering volumes for a given sample viscosity. To demonstrate the broad applicability, several model systems are measured with CRSANS, including silica nanoparticle suspensions, NIST monoclonal antibodies, and worm-like micelle (WLM) surfactant solutions. The built-in capability to perform high-throughput sample mixing and SANS contrast variation is also demonstrated. Lastly, more detailed CRSANS measurements of WLM surfactant solutions are compared with the rotating concentric-cylinder geometry (RheoSANS) and the rectangular-slit geometry (μRheoSANS) to validate the rheological and nanostructural measurements.

2 Materials and Methods

2.1 Capillary rheometry

The setup and key components of CRSANS are summarized in Fig. 1. In Fig. 1a, an incident neutron beam scatters off the silica capillary coil (Fig. 1b) that contains the flowing sample (Fig. 1c). Calculations of the shear stress and shear rate assume that the flow field is axisymmetric at $r = 0$ and constant along the capillary length axis z. Coiling the capillary increases the scattering volume by a factor $2N_c$, in which N_c is the number of circular loops. The coil diameter $D_c \approx 30$ mm is significantly larger than the capillary inner diameter $D \approx 0.1$ mm, which limits the effect of curvature on the sample flow profile.

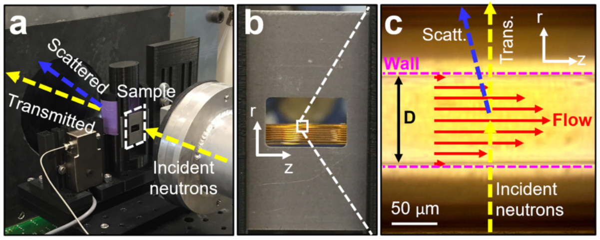

Fig. 1 (a) Capillary RheoSANS (CRSANS) sample environment at the NIST Center for Neutron Research NGB-10m SANS beamline. (b) Front image of the capillary coil that is arranged perpendicular to the incident neutron beam. (c) The fused silica capillary with horizontal flow of the sample along the capillary z-axis.

The flexible capillaries were purchased from Molex (Polymicro Capillary Tubing, type VS and TSP). Capillaries consist of a fused silica wall and a thin polyimide coating (≈ 20 μm) to limit scratching and breakage of the silica wall. According to the manufacturer, the interior fused silica surface should be mirror smooth with a root-mean-square surface roughness less than ≈ 7 nm. Capillary inner diameters (D) can range from 0.2 μm to 700 μm, while outer diameters (OD) can range from approximately 360 μm to 850 μm. Tolerances in D range from approximately 1% (± 1 μm, VS type) to 6% (± 10 μm, TSP type). Capillaries are cut manually to the desired length by using a cleaving stone to penetrate the polyimide coating and then separated by pulling axially. Capillary lengths (L) for CRSANS measurements can feasibly vary from 30 mm up to 5000 mm. Immediately after cleaving, both capillary ends are rinsed with ethanol to remove residual glass debris. Small glass debris can scratch the interior surface and lead to capillary breakage at high pressures.

High pressure liquid pumps are used for unidirectional flow (Dionex P-580 dual piston pumps) and reciprocating flow configurations (Cetoni neMESYS high pressure syringe pumps). Capillaries are directly connected to flow-through pressure sensors (DJ Instruments, type DF2-High Pressure), which are used to measure the pressure drop along the capillary. For unidirectional flow, a pressure sensor is connected only to the capillary inlet. For reciprocating flow, pressure sensors are connected to the capillary inlet and outlet.

Tubing connections between the pumps, pressure sensors, and flow selector valves contain stainless steel compression fittings with 10-32 coned ports and stainless steel tubing with 1/16 inch (1.6 mm) outer diameter. Connections between the fused silica capillaries and the pressure sensors require adapter fittings (Prolab Instruments, UHPLC fittings) for the capillary outer diameter (360 μm) and the compression fitting diameter (1/16 inch or 1.6 mm). The Electronic Supplemental Information (ESI) contains additional information regarding the experimental setup (ESI, Fig. 1), sensor calibrations (ESI, Fig. 2), and the various corrections used for the capillary rheometry of non-Newtonian fluids (ESI, Fig. 3).†

The shear stress evaluated at the wall σ_w is defined as,[17]

$$\sigma_w = \frac{(\Delta P - P_{end})R}{2L} \tag{1}$$

where ΔP is the pressure drop along the capillary, L is the capillary length, R is the capillary inner radius ($R = D/2$), and P_{end} is any additional pressure drop due to end effects.[18] Here, capillaries are sufficiently long $L/R \gg 1000$, such that end effects terms are negligible and $P_{end} = 0$. When end effects contribute a significant pressure drop, P_{end} can be determined using the Bagley method[17] by repeating measurements with varying L/R (ESI,† Fig. 3).

The apparent shear rate at the capillary wall $\dot{\gamma}_w^a = 4Q(\pi R^3)^{-1}$ is corrected for apparent wall slip using the Mooney method,[17]

$$\dot{\gamma}_w^c = \frac{4Q}{\pi R^3} - \frac{4v_{slip}}{R} \tag{2}$$

where $\dot{\gamma}_w^c$ is the slip-corrected shear rate, Q is the measured volumetric flow rate, and v_{slip} is the apparent slip velocity at the wall. The apparent slip velocity is determined by repeating measurements with varying R. Measurements in this work primarily used capillaries with $R = 50$ μm, and the effect of wall slip was a relatively small correction (5%). However, the effect of wall slip can become significant for smaller capillaries (50% correction, ESI,† Fig. 3).

Slip-corrected shear rates at the wall are further corrected for non-parabolic flow profiles using the Weissenberg-Rabinowitsch method,[17]

$$\dot{\gamma}_w = \dot{\gamma}_w^c \left[\frac{1}{4}\left(3 + \frac{d\ln\dot{\gamma}_w^c}{d\ln\sigma_w}\right)\right]. \tag{3}$$

in which $\dot{\gamma}_w$ is now assumed to be the *true* shear rate at the wall.

The true sample viscosity η is given by the ratio of the shear stress at the wall (Eq. 1) and true shear rate at the wall (Eq. 3),

$$\eta = \frac{\sigma_w}{\dot{\gamma}_w} \tag{4}$$

2.2 Flow instabilities

The ratio of inertial forces to viscous forces is given by the dimensionless Reynolds number,

$$Re = \frac{\rho D v_{avg}}{\eta} \tag{5}$$

in which ρ is the solution density, $v_{avg} = 4Q(\pi D^2)^{-1}$ is the average fluid velocity, D is capillary inner diameter, and η is the sample viscosity. To estimate the maximum Re for non-Newtonian samples, η is assumed to be the infinite shear viscosity η_∞ or the solvent viscosity η_0. For straight capillaries, the flow typically transitions from laminar to turbulent approximately when $Re > 2000$.[17]

A single capillary is coiled with a diameter D_c to maximize the capillary volume located within the neutron beam path. Secondary flows can develop in a coiled capillary due to the additional inertia-derived force due to the wall curvature that points outward from the coil center. The dimensionless Dean number (Dn) accounts for this additional force due to the wall curvature, which is defined as[19]

$$Dn = Re\sqrt{D/D_c} \tag{6}$$

where D_c is the coil diameter. Here, the ratio of capillary to coil diameter is small ($D/D_c < 0.01$). When $Dn < 30$ and $D/D_c \ll 1$, the inertial and centrifugal forces are negligible, and the flow primarily resembles unidirectional flow velocity along the z-axis.[19] In this case, the same equations described in the previous section for a straight capillary are valid for a coiled capillary. Secondary flows grow significantly in the approximate range of $30 < Dn < 400$, and the flow eventually becomes turbulent when $Dn > 400$.[19,20]

2.3 Adjustable capillary configurations

A key advantage of CRSANS is the ability to easily switch between a broad selection of capillary diameters and lengths to optimize the experimental setup for each sample. The constrained optimization of capillary configurations depends on the sample viscosity, the pump flow rates, the pressure limitations, the desired maximum $\dot{\gamma}_w$, and the desired scattering count times. For each sample, there will be a trade-off between maximizing the wall shear rate and maximizing the scattering volume. Any given capillary configuration can be altered to increase the maximum wall shear rate by decreasing the scattering volume.

In Fig. 2a, the range of shear rates at the wall (left axis) and the normalized scattering volume (right axis) are shown for one example capillary configuration. In this example, the maximum curves (blue circles) and the minimum curves (red squares) are determined by the pressure and flow rate limitations of the pump and sensors. The current pressure limits are $P_{min} = 0.1$ bar and $P_{max} = 500$ bar, and the current flow rate limits are $Q_{min} = 4$ nL min^{-1} and $Q_{max} = 21$ mL min^{-1}. The green area between these two curves represents the obtainable range of shear rates for each D at a fixed viscosity ($\eta = 1$ mPa-s), fixed capillary length ($L = 1000$ mm), and fixed coil diameter ($D_c = 30$ mm). Meanwhile, the orange diamond symbols (right axis) correspond to the normalized scattering volume for the same capillary coil. To provide a practical reference, the normalized scattering volume is defined as V_{scatt}/V_{ref}, in which V_{scatt} is the capillary volume within the neutron beam path, and V_{ref} is a typical SANS scattering volume ($V_{ref} = 104$ μL). The count times for CRSANS experiments are typically $10-100$ times greater than static SANS measurement, which is comparable to other small-volume experiments using polymer thin films[21] or the 1-2 shear cell.[22]

For maximum $\dot{\gamma}_w$ at fixed L and fixed η, the optimal D coincides at the intersection of the maximum pump pressure and flow rate curves (blue circles). However, this D is not necessarily the best choice to maximize the scattering volume at a different shear rate constraint. For example, under the shear rate constraint $\dot{\gamma}_w \geq 10^6$ s^{-1} and volume constraint $V_{scatt}/V_{ref} \geq 1\%$, the optimal configuration coincides at $D = 100$ μm, $L = 1000$ mm, $\eta = 1$ mPa-s (vertical magenta line). If instead the shear rate constraint is relaxed to $\dot{\gamma}_w \geq 10^5$ s^{-1}, then the optimal D to maximize scattering volume coincides instead near $D = 200$ μm with $L = 3000$ mm, which increases the total scattering volume by a factor of 100.

Secondary flows and flow instabilities remain another important consideration for each experiment. The onset for turbulence is predicted by the the Reynolds number for a straight capillary (Eq. 5) and the Dean number for a coiled capillary (Eq. 6). In Fig. 2b, the blue circles correspond to Re (left axis), while the red diamonds correspond to Dn (right axis) at a fixed coil diameter $D_c = 30$ mm. At the maximum shear rate, the same sample is predicted to remain laminar in a straight capillary ($Re \leq 1500$), but should produce secondary flows due to curvature at the maximum shear rate ($Dn \approx 100$).[19] If secondary flows are undesirable, a smaller inner diameter ($D = 50$ μm or 75 μm) or a larger coil diameter ($D_c = 50$ mm) should be used instead such that $Dn < 30$. Consequently, decreasing D will also decrease $\dot{\gamma}_w^{max}$ and V_{scatt}/V_{ref}, as shown in Fig. 2a.

Example capillary configurations are summarized in Tab 1 for different infinite shear viscosity η_∞. The calculations assume a maximum pressure drop of $\Delta P = 500$ bar, a maximum flow rate of $Q = 21$ mL min^{-1}, and a coil diameter $D_c = 30$ mm.

Table 1 Example operating conditions for different capillary geometries

η_∞ (mPa-s)	D (μm)	L (mm)	$\dot{\gamma}_w^{max}$ (s^{-1})	V_{scatt}/V_{ref} (%)	Re
1	50	600	1.0×10^6	0.2	326
1	100	1000	1.3×10^6	1.8	1563
1	200	3000	4.5×10^5	23.6	2228
5	150	350	1.1×10^6	0.9	594
5	200	3000	1.7×10^5	23.6	167
10	150	200	9.4×10^5	0.4	264
10	300	3000	1.3×10^5	53.0	141
100	250	250	1.3×10^5	1.2	10
100	300	3000	1.3×10^4	53.0	1.4
1000	500	600	1.0×10^4	24.5	0.3

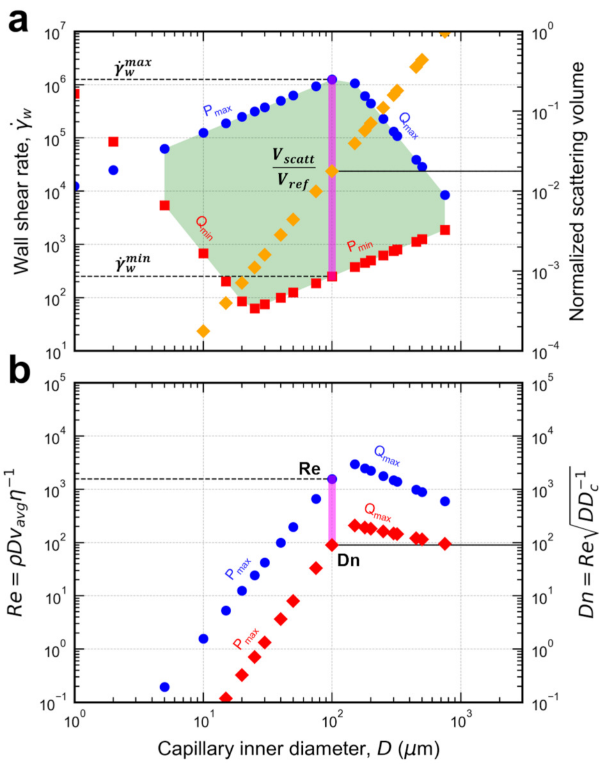

Fig. 2 (a) Example operating conditions with a maximum shear rate (blue circles, left axis) and minimum shear rate (red squares, left axis) defined by the pump pressure and flow rate limitations. The corresponding normalized scattering volume V_{scatt}/V_{ref} is given at the right axis (orange diamonds). In this example, the capillary length ($L = 1000$ mm), sample viscosity ($\eta = 1$ mPa-s), and coil diameter ($D_c = 30$ mm) are fixed. (b) Corresponding maximum Reynolds number (left axis) and maximum Dean number (right axis) for the same specifications in (a).

2.4 Small-angle neutron scattering (SANS)

SANS measurements were performed at the NIST Center for Neutron Research at the the NGB10m SANS, NGB30m SANS, and NG3 VSANS beamlines.[23] The neutron detectors and guides were configured to maximize neutron flux while spanning a q-range of approximately 0.01 Å $< q <$ 0.3 Å, where $q = 4\pi\lambda^{-1}\sin(\theta/2)$, λ is the neutron wavelength, and θ is the scattering angle. Sample count times typically ranged from 10 min to 100 min. All SANS data were reduced using available reduction procedures.[24]

In addition to the sample scattering, significant anisotropic scattering occurs from the aligned capillaries in the beam path. Scattering from the capillary cell appears above the incoherent background at approximately $q < 0.01$ Å, and follows a Porod scattering dependence $I(q) \sim q^{-4}$. To correct for the capillary scattering, the empty cell measurement consisted of a capillary filled with a mixture of hydrogenated solvent (e.g. H_2O) and deuterated solvent (e.g. D_2O) that matched the volume-average scattering length density (SLD) of the sample. The SLDs of the h/d-solvent mixture and the sample of interest was calculated using an available online database.[25] In this manner, the empty cell and sample scattering contain the same volume-averaged SLD outside the capillary (air) and inside the capillary (h/d-solvent).

In general, the scattering intensity of a monodisperse, two component system of particles (p) in a solvent (s) can be written as

$$I(q) = \phi_v[\rho_p - \rho_s]^2 P(q)S(q) + B \tag{7}$$

in which ϕ_v is the volume fraction of particles, ρ_p and ρ_s are the SLDs of the particle and solvent, respectively, B is the incoherent background scattering, $P(q)$ is the orientation-averaged particle form factor that describes the particle size and shape, and $S(q)$ is the structure factor that describes the relative particle positions based on their interparticle interactions. Scattering models and functions were fit to the SANS measurements using SasView.[26] A polydisperse spherical form factor model and the Hayter-Penfold structure factor model were combined using SasView to fit the scattering data of charged silica nanoparticles in water.[26] The degree of alignment for worm-like micelle dispersions was quantified by an alignment factor (AF), which was determined by fitting a Legendre polynomial expansion function to the scattered intensity at the slice position $q_p = 0.025 \pm 0.005$ Å^{-1} as a function of the azimuthal angle (ϕ).[5,27] Note that the alignment factor is equivalent to the parameter P_2 from the second coefficient. In the limit when $AF = 0$, a collection of rods are isotropically distributed with no favored orientation. In the limit when $AF = 1$, a collection of rods are entirely aligned along the direction of flow.[5,27]

To isolate the near-wall scattering, the same general procedure applied with the rectangular geometry is applicable to the cylindrical geometry.[5] This analysis requires that the shear stress varies linearly from the center-line ($r = 0$) to the wall ($r = R$) at each flow rate Q. Given the scattered intensity I_n and I_{n-1} at two specified flow rates Q_n and Q_{n-1}, respectively, the scattered intensity can be decomposed as,

$$I_n(q_x, q_y) = [1 - s]I_{near-wall}(q_x, q_y) + [s]I_{n-1}(q_x, q_y) \tag{8}$$

in which q_x and q_y are the horizontal and vertical components of scattering vector q, respectively, $I_{near-wall}$ is the isolated scattering intensity near the wall, and s is a weighting constant calculated from the wall stress. For a cylindrical geometry, $s = (\sigma_{w,n-1}/\sigma_{w,n})^2$, where $\sigma_{w,n}$ and $\sigma_{w,n-1}$ are the wall stresses measured at flow rates Q_n and Q_{n-1}, respectively. Rearranging Eq. 8 for the scattered intensity near the wall gives,

$$I_{near-wall}(q_x, q_y) = [1 - s]^{-1}\left[I_n(q_x, q_y) - sI_{n-1}(q_x, q_y)\right] \tag{9}$$

As demonstrated previously for a rectangular slit geometry, Eq. 9 applies with $s = \sigma_{w,n-1}/\sigma_{w,n}$.[5] In a rectangular slit geometry, the scattering is a projection of the 1-3 plane (velocity-vorticity plane). In a cylindrical capillary geometry, the resulting scattering is a combined projection of planes varying between the 1-3 plane and the 1-2 plane (velocity-velocity gradient plane). This is an important consideration when comparing the structural measurements of complex fluids using different flow geometries.

3 Results and Discussions

3.1 Probing the nanostructure of complex fluids

In Fig. 3, three different model systems were measured to demonstrate the broad capabilities of CRSANS, which consist of (a) silica nanoparticles, (b) monoclonal antibodies (mAbs), and (c) worm-like micelle (WLM) surfactants. Details regarding sample preparation are described in the ESI.† Error bars represent one standard deviation and may be smaller than the symbol size.

The measured scattering intensities $I(q)$ from concentrated ≈ 30 nm silica nanoparticle suspensions at 21% (blue squares) and 36% by volume (red circles) are shown in Fig. 3a. The black lines represent the model fits using a polydisperse sphere form factor and a charged sphere structure factor in SasView.[26] The insets show $2D$ SANS patterns of silica suspensions at 21% by volume under quiescent conditions with $\dot{\gamma}_w = 0$ s^{-1} (top right) and under high shear conditions with $\dot{\gamma}_w \approx 10^5$ s^{-1} (bottom left). Anisotropy in the $2D$ scattering pattern was most noticeable in the direction perpendicular to flow (yellow arrows), which indicated that the suspension microstructure was changed due to hydrodynamic interactions at sufficiently high shear rate. More specifically, the randomized structure generated by Brownian motion was altered due to the imposed flow field when the Péclet number exceeded unity ($Pe = 6\pi\eta a^3\dot{\gamma}_w/kT$), where Pe represents the ratio of the characteristic hydrodynamic effects to Brownian diffusivity, a is the particle radius, and kT is the Boltzmann energy. The anisotropic scattering pattern was qualitatively consistent with hydrodynamic simulations of concentrated hard spheres in pipe flow in the limit $Pe \to \infty$.[28]

The relatively small sample volume required to operate CRSANS (≈ 2 mL) makes it amenable to measuring supply-limited samples, including deuterated and biological samples. As one example of a supply-limited biological sample, a concentrated suspension of the NIST monoclonal antibody (NISTmAb) is shown in Fig. 3b. Approximately 2 mL of NISTmAb solution at 25 mg mL^{-1} was continuously sheared at $\dot{\gamma}_w \approx 10^6$ s^{-1} for 20 h (blue symbols). The same sample was then sheared and heated at ≈ 40 °C for an additional 40 h (red symbols). A noticeable increase in the intensity at low q was observed after sufficiently long shearing and heating (Fig. 3b inset), which indicated the formation of larger mAb aggregates. Interestingly, the suspension became visibly turbid prior to the low-q increase measured with SANS. This observation suggests the mAb aggregates were large (> 1 μm) and formed at low concentration relative to the overall protein concentration. The $2D$ scattering remained isotropic at the highest examined shear rate, indicating that the aggregation process was not *only* due to changes in the hydrodynamic interactions imposed by shearing. Instead, it is hypothesized that the interfacial contact between the mAbs and the system boundaries served as nucleation sites for the growth of protein aggregates. Ongoing work aims to distinguish the mechanism of mAb protein aggregation to improve the solution lifetime within the processing pipeline.

Lastly, self-assembled worm-like micelles (WLMs) were measured with CRSANS, as shown in Fig. 3c. The WLMs consist of sodium lauryl ether sulfate (SLES) at 1.2%, 2.3%, and 4.6% by mass in a brine solution of D_2O and NaCl (8% NaCl by mass). Previous reports indicate these WLMs have a diameter $D \approx 4.2$ nm and persistence length $L_p \approx 28$ nm.[5] The 2D SANS pattern is shown in the inset for WLMs at 4.6% by mass under quiescent conditions (left) and flowing conditions (right, $\dot{\gamma}_w \approx 10^4$ s^{-1}). As shown in the inset, the 2D scattering becomes highly anisotropic

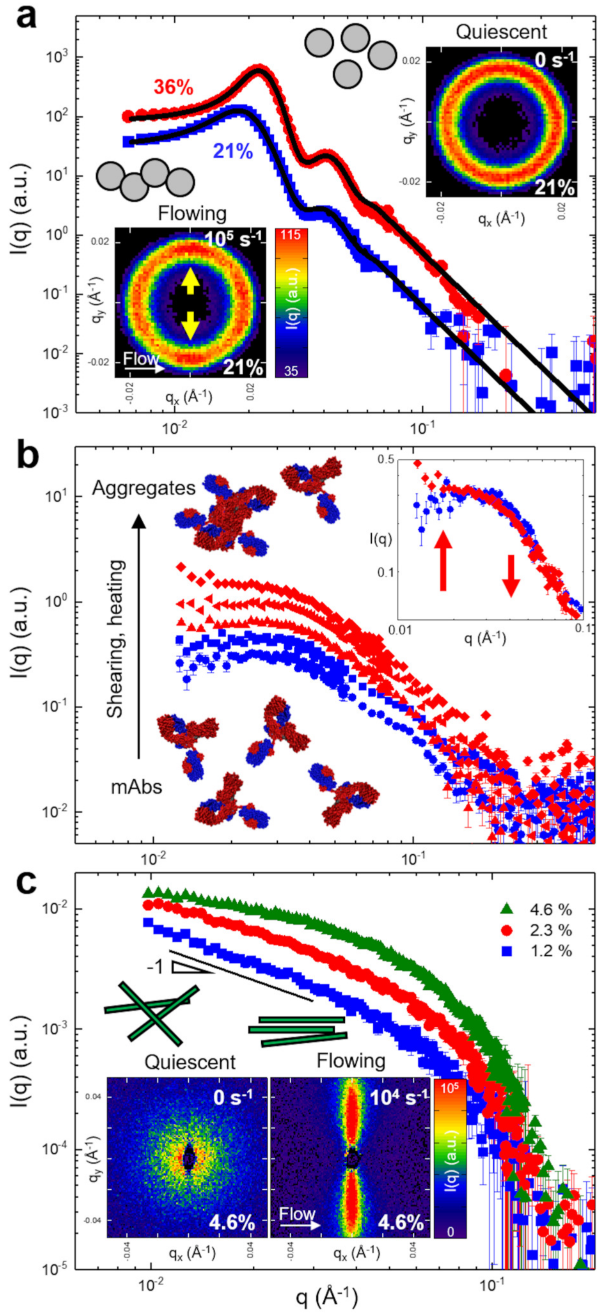

Fig. 3 CRSANS measurements of different model systems. (a) Charge-stabilized silica nanoparticles at 21% (blue squares) and 36% by volume (red circles). Insets show 2D scattering for the 21% by volume suspension at rest (top right) and flowing conditions (bottom left) with $\dot{\gamma}_w \approx 10^5$ s^{-1}. (b) NISTmAb solution with increasing time (bottom to top) over 60 hours at $\dot{\gamma}_w \approx 10^6$ s^{-1} without heating (blue circles at 0 h, squares at 20 h) and with heating (red upward triangles at 23 h, left triangles at 27 h, diamonds at 60 h). Data are vertically shifted from top to bottom by 4.5, 3, 2, 1.4, and 1 for clarity. The inset shows the intensity increase at low q from the beginning (circles) to end (diamonds). (c) Worm-like micelles at 4.6% (green triangles), 2.3% (red circles), and 1.2% by mass (blue squares). Insets show 2D scattering at rest (left) and flowing (right) with $\dot{\gamma}_w \approx 10^4$ s^{-1}. The incoherent background scattering B has been subtracted from $I(q)$ for all scattering data.

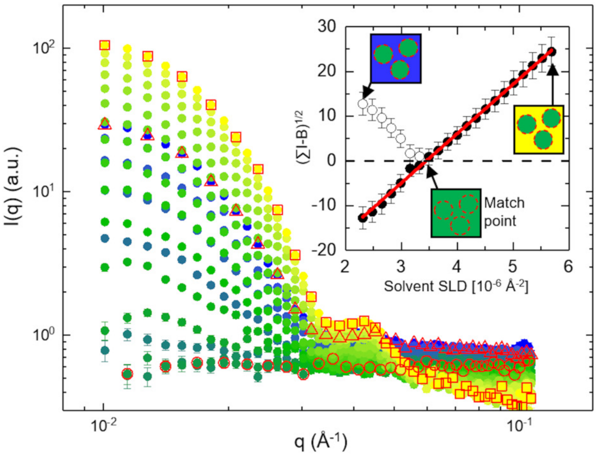

Fig. 4 High-throughput mixing and SANS measurements of dilute suspensions containing silica nanoparticles with varying mixture composition of H_2O-rich solvent (blue symbols) and D_2O-rich solvent (yellow symbols). Inset shows the square root of the integrated coherent scattering intensity as a function of the calculated solvent SLD.

as micelles strongly align along the horizontal direction of flow.

3.2 High-throughput mixing and contrast variation

The CRSANS device is capable of dynamically mixing two or more sample feeds together prior to injection into the sample cell. This built-in mixing capability can be used to perform high-throughput contrast variation, such as the example demonstrated in Fig. 4. $I(q)$ was measured for dilute silica nanoparticles ($\approx 1\%$ by volume) dispersed in different solvent mixtures of H_2O and D_2O, where the changing color scale from blue-green-yellow represents increasing D_2O concentration at fixed silica concentration.

In this example, the solvent gradient is produced continuously using two pumps connected to a dynamic mixer (ESI,† Fig. 1d). The scattering and transmission measurements of 20 samples are mixed and measured in ≈ 100 minutes. The scattering length density (SLD) contrast between the silica particles and solvent changes significantly as silica in H_2O-rich solvent mixes with silica in D_2O-rich solvent. The coherent scattering intensity is at a minimum at the contrast-match point (green circles with red outline), and only the incoherent background scattering (B) remains when the volume-averaged solvent SLD equals the particle SLD ($\rho_s = \rho_p$ in Eq. 7). In the inset of Fig. 4, the square root of the integrated coherent scattering intensity is plotted as a function of the calculated solvent SLD. The contrast match point occurs when the solvent SLD equals the particle SLD and $[\Sigma(I-B)]^{1/2} = 0$. Note that the data shown as open circles have been mirrored on the $y = 0$ axis (dashed line) to allow linear regression using all data points (red solid line). The particle SLD obtained from linear interpolation is $3.5 \pm 0.1 \times 10^{-6}$ Å^{-2}, which agrees with values obtained from other rapid contrast variation techniques using microfluidics.[13]

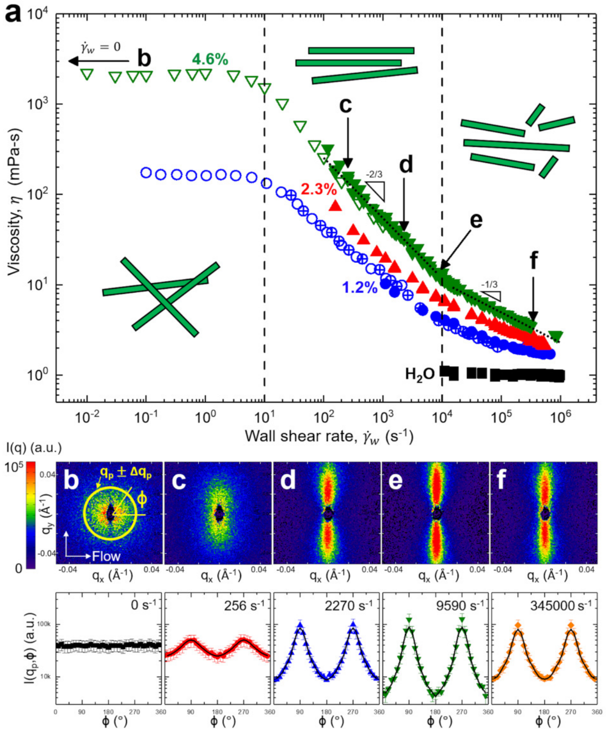

Fig. 5 (a) Steady-shear viscosity measurements of WLMs at (down triangles) 4.6 %, (triangles) 2.3 %, and (circles) 1.2 % by mass. The measured viscosity of H_2O is shown as black squares. Different measurement geometries are compared between this work using (closed symbols) CRSANS, (open symbols) rotational concentric cylinders, and previous measurements using (crossed circles) rectangular slit μRheoSANS.[5] The corresponding 2D SANS patterns are shown below at different $\dot{\gamma}_w$ from (b) 0 s^{-1}, (c) 1.7×10^2 s^{-1}, (d) 1.7×10^3 s^{-1}, (e) 1.7×10^4 s^{-1}, and (f) 1.7×10^5 s^{-1}. The corresponding bottom graphs include the measured $I(q_p,\phi)$ (symbols) as a function of azimuthal angle ϕ at the peak $q_p = 0.025 \pm 0.005$ Å^{-1}, and the Legendre function fit (lines) used to obtain the alignment factor.

3.3 Linking the rheology and nanostructure

To further examine the link between rheology and nanostructure, this section focuses on the model WLM suspensions reported above in section 3.1 (SLES in NaCl-D_2O brine). In Fig. 5a, the steady-shear viscosity is shown as a function of the wall shear rate $\dot{\gamma}_w$ over eight orders of magnitude from 10^{-2} s^{-1} to 10^6 s^{-1}. The viscosity is measured using different methods and geometries, including a rotating concentric cylinder geometry from traditional RheoSANS (open symbols), a rectangular slit geometry from previous μRheoSANS (crossed circles),[5] and the capillary geometry from this work (closed symbols). Strong shear-thinning behavior is observed when $\dot{\gamma}_w > 10$ s^{-1} for all WLM concentrations from 1.2% (blue circles), 2.3% (red up triangles), and 4.6% by mass (green down triangles). For reference, measurements of pure H_2O are shown as black squares.

In Fig. 5b-f, the corresponding 2D SANS patterns (top) and azimuthal dependence (bottom) are shown for various wall shear rates denoted by arrows in Fig. 5a. For reference, the flow direction is parallel to q_x (x-axis) and is perpendicular to q_y (y-axis). As $\dot{\gamma}_w$ increases, the scattering anisotropy increases up to a critical shear rate (e) at $\dot{\gamma}_w \approx 10^4$ s^{-1}. This increase in anisotropic scattering is directly related to changes in the orientation distribution function of worm-like micelles, in which an increase in the intensity perpendicular to the flow direction (q_y) corresponds to alignment of WLMs along the flow direction (q_x).

Above the critical shear rate of $\dot{\gamma}_w \approx 10^4$ s^{-1}, the scattering anisotropy *decreases* with increasing $\dot{\gamma}_w$. We speculate the decrease in micelle alignment occurs as hydrodynamic forces physically break apart the worm-like micelles into shorter rods. Interestingly, this maximum in scattering anisotropy coincides with the change in power-law scaling of the viscosity. Below this critical rate, the viscosity decreases and scales as $\eta \sim \dot{\gamma}^{-2/3}$. Above this critical rate, the viscosity decreases and scales as $\eta \sim \dot{\gamma}^{-1/3}$. The change in power-law slope from $-2/3$ to $-1/3$ is consistent with recent measurements of different worm-like micelle surfactant systems[18] and is consistent with the transition of flexible, worm-like micelles into shorter rod-like micelles.[18,29–32]

Although the viscosity continued to decrease up to $\dot{\gamma}_w \approx 10^6$ s^{-1}, the steady-shear viscosity is expected to eventually become shear-independent and plateau at an infinite shear viscosity (η_∞). Ongoing work aims to generate higher shear rates up to 10^7 s^{-1} with CRSANS to further test this hypothesis by directly measuring η_∞.

To quantify the degree of scattering anisotropy, an alignment factor (AF) was determined by fitting an even Legendre polynomial expansion to the scattered intensity at $q_p = 0.025 \pm 0.005$ Å^{-1} as a function of the azimuthal angle (ϕ) and extracting the parameter P_2 from the second coefficient.[27] The limit $AF = 0$ corresponds to an isotropic distribution of rods, while the limit $AF = 1$ corresponds to perfectly aligned distribution along the flow direction. In Fig. 6a, the alignment factor is shown for WLM suspension at 4.6% by mass obtained from SANS measurements using the entire capillary volume (green down triangles). This alignment factor accounts for an average over the entire scattering volume, which is weighted toward the volume near the wall according to Eq. 8. In this case, a maximum alignment factor $AF \approx 0.65$ occurs at $\dot{\gamma}_w \approx 2 \times 10^4$ s^{-1}.

Following previous methods for pressure-driven flows[2] and μRheoSANS,[5] scattering near the wall can be isolated by subtracting two measurements of the same sample at different flow rates. The scattered intensity in this isolated near-wall region $I_{near-wall}(q_x, q_y)$ is calculated using Eq. 9, which weights the measured scattered intensities by the ratio of shear stresses evaluated at the wall. This subtraction method assumes that the shear stress varies linearly from zero at the center-line $\sigma(r = 0) = 0$ to the maximum stress at the wall $\sigma(r = R) = \sigma_w$. The method to isolate the high shear region near the capillary wall is demonstrated in Fig. 6b-d. The near-wall scattering $I_{near-wall}$ in (d) is obtained by weighting and subtracting the measured intensity at higher shear rates I_n in (b) and lower shear rates I_{n-1} in (c). Note that $I_{near-wall}$ still contains a reduced range of shear rates, which spans from the wall shear rate in (b) to the wall shear rate in (c). In Fig. 6a, the black right-filled triangles correspond to alignment factors obtained from subtracted capillaries, and the left error bars correspond to the isolated shear rate ranges. For comparison, the alignment factors obtained by traditional RheoSANS methods in a rotating concentric cylinder geometry are shown as open circles.

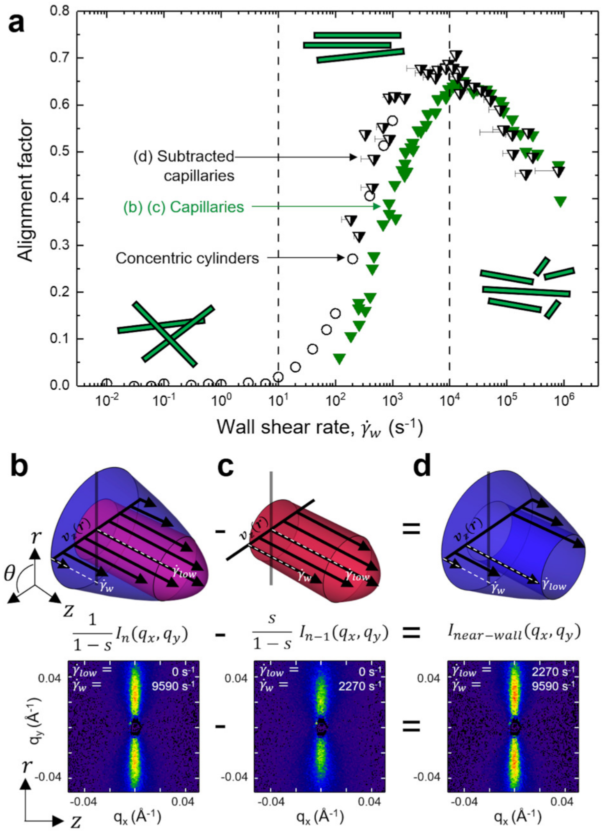

Fig. 6 (a) Alignment factors obtained from SANS measurements of WLMs at 4.6% SLES by mass. Alignment factors are compared for the full capillary geometry (green triangles), the isolated high shear region in the subtracted capillaries (right-filled triangles), and the concentric cylinder geometry (open circles). The isolated region near the capillary wall is obtained from Eq. 9, as demonstrated graphically in (b-d). The stress-weighted difference in (d) $I_{near-wall}$ is obtained by subtracting measurements at a higher wall shear rate (b) and at a lower wall shear rate (c). In this example, the shear rate range for the near-wall region spans from 2270 s^{-1} to 9590 s^{-1} or $\dot{\gamma}_w$ in (c) and (b), respectively.

Prior to isolating the scattering near the capillary wall, there are obvious differences in the AF obtained from scattering measurements in the concentric cylinders and the full capillaries. In the case of concentric cylinder geometry, there is a constant shear rate across the gap, and thus the entire sample microstructure experiences a constant shear stress. Meanwhile, in the capillary geometry, there is a range of shear rates across R, and thus the sample microstructure experiences a range of shear stresses from a maximum at the wall to zero at the center-line.

After isolating the high shear region, the maximum alignment factor was approximately $AF = 0.68$ at $\dot{\gamma} \approx 8 \times 10^3$ s^{-1}, as shown in Fig. 6a (right-filled triangles). Good agreement is found between AF obtained from concentric cylinders and the subtracted capillaries in the overlapping region from approximately 10^2 s^{-1} to 10^3 s^{-1}. Thus, CRSANS serves as a unique method to significantly extend the traditional RheoSANS methods toward higher shear rates in order to better understand the link between shear-dependent nanostructure and rheological behavior. By combining CRSANS and rotational RheoSANS methods, the rheology and nanostructure of complex fluids can be measured over eight orders of magnitude in shear rate ranging from $\dot{\gamma}_w \approx 10^{-2}$ s^{-1} to 10^6 s^{-1}.

4 Conclusions

Capillary RheoSANS combines a capillary rheometer with small-angle neutron scattering to simultaneously measure the rheology and nanostructure of complex fluids at high shear rates. CRSANS configurations can be adjusted to the desired maximum shear rate and scattering volume using a wide range of capillary inner diameters from $D \approx 0.2$ μm to 700 μm, capillary lengths from $L \approx 30$ mm to 5000 mm, and flow rates from $Q \approx 4$ nL min^{-1} to 21 mL min^{-1}. By combining capillary and rotational RheoSANS techniques, the nanostructure and rheology of complex fluids can be measured over eight orders of magnitude in shear rate from $\dot{\gamma}_w \approx 10^{-2}$ s^{-1} to 10^6 s^{-1}.

The broad applicability of CRSANS was demonstrated by measuring a variety of model systems, including chaining of silica nanoparticles, aggregation of NIST monoclonal antibodies, and alignment of worm-like micelles. These nanostructural changes were observed at shear rates above 10^4 s^{-1}, which are inaccessible with current rotational RheoSANS techniques.

To obtain maximum wall shear rates in excess of 10^6 s^{-1}, CRSANS is currently limited to samples with an infinite shear viscosity of less than 10 mPa-s. Above this viscosity limit, the capillary length and diameter must be reduced to the extent where the normalized scattering volume becomes impractical for neutron scattering ($V_{scatt}/V_{ref} < 0.001$). In the case of exceedingly small scattering volumes ($V_{scatt} < 100$ nL), we anticipate that the transparent capillary rheometer could be modified for X-ray or light scattering techniques to provide feasible measurement times using higher incident photon flux. The transparent capillary is also suitable to visualize the flow profile using microscopy and particle image velocimetry,[18,33,34] although further development is needed to accurately track the velocity profile at $\dot{\gamma}_w \approx 10^6$ s^{-1}.

This work highlights the applicability of high shear capillary rheometry with small-angle neutron scattering techniques. Ongoing developments aim to expand the lower and upper shear rate bounds, to provide temperature control, and to improve the measurement of high-viscosity samples such as polymer melts, pastes, and slurries. Overall, CRSANS will expand the nanoscale measurement of alignment, aggregation, and breakdown of complex fluids, which may lead to macroscopic changes in the material properties at industrially-relevant shear rates.

Conflicts of interest

There are no conflicts to declare.

5 Acknowledgements

Access to the NGB30 SANS and NG3 VSANS instruments was provided by the Center for High Resolution Neutron Scattering, a partnership between the National Institute of Standards and Technology and the National Science Foundation under Agreement No. DMR-1508249. Portions of this work benefited from and provided support to the NIST nSoft consortium, including use of the 10 meter SANS instrument at the NCNR. This work benefited from the use of the SasView application, originally developed under NSF award DMR-0520547. SasView contains code developed with funding from the European Union's Horizon 2020 research and innovation programme under the SINE2020 project, grant agreement No 654000. RPM acknowledges funding from the National Research Council (NRC) Research Associateship Program (RAP). The authors thank Nicos Martys, Yun Liu, Elizabeth Kelley, and Paul Butler for helpful discussions. Commercial equipment and materials identified in this work do not imply recommendation nor endorsement by the National Institute of Standards and Technology.

Notes and references

1 S. J. King and S. D. Price, *J Chem Phys*, 2007, **127**, 174307.
2 L. Fernandez-Ballester, D. W. Thurman and J. A. Kornfield, *Journal of Rheology*, 2009, **53**, 1229–1254.
3 A. P. R. Eberle and L. Porcar, *Current Opinion in Colloid Interface Science*, 2012, **17**, 33–43.
4 C. G. Lopez, T. Watanabe, M. Adamo, A. Martel, L. Porcar and J. T. Cabral, *J Appl Crystallogr*, 2018, **51**, 570–583.
5 J. S. Weston, D. P. Seeman, D. L. Blair, P. F. Salipante, S. D. Hudson and K. M. Weigandt, *Rheologica Acta*, 2018, **57**, 241–250.
6 J. J. Richards and J. K. Riley, *Current Opinion in Colloid Interface Science*, 2019, **42**, 110–120.
7 A. Bharati, S. D. Hudson and K. M. Weigandt, *Current Opinion in Colloid Interface Science*, 2019, **42**, 137–146.
8 P. T. Corona, N. Ruocco, K. M. Weigandt, L. G. Leal and M. E. Helgeson, *Sci Rep*, 2018, **8**, 15559.
9 V. Lutz-Bueno, J. Kohlbrecher and P. Fischer, *Journal of Non-Newtonian Fluid Mechanics*, 2015, **215**, 8–18.
10 L. Porcar, D. Pozzo, G. Langenbucher, J. Moyer and P. D. Butler, *Rev Sci Instrum*, 2011, **82**, 083902.
11 J. Kim and M. E. Helgeson, *Physical Review Fluids*, 2016, **1**, year.
12 C. G. Lopez, T. Watanabe, A. Martel, L. Porcar and J. T. Cabral, *Sci Rep*, 2015, **5**, 7727.
13 M. Adamo, A. S. Poulos, R. M. Miller, C. G. Lopez, A. Martel, L. Porcar and J. T. Cabral, *Lab Chip*, 2017, **17**, 1559–1569.
14 A. K. Van Dyk, T. Chatterjee, V. V. Ginzburg and A. I. Nakatani, *Macromolecules*, 2015, 150304160530000.
15 T. Chatterjee, A. I. Nakatani and A. K. Van Dyk, *Macromolecules*, 2014, **47**, 1155–1174.
16 J. C. Lee, K. M. Weigandt, E. G. Kelley and S. A. Rogers, *Phys Rev Lett*, 2019, **122**, 248003.
17 C. W. Macosko, *Rheology: Principles, Measurements, and Applications*, Wiley-VCH, Inc., 1994.
18 P. F. Salipante, V. L. Dharmaraj and S. D. Hudson, *Journal of Rheology*, 2020, **64**, 481–492.
19 S. A. Berger, L. Talbot and L. S. Yao, *Annu Rev Fluid Mech*, 1983, **15**, 461–512.
20 G. I. Taylor, *Proceedings of the Royal Society of London A: Mathematical, Physical and Engineering Sciences*, 1929, **124**, 243–249.
21 H. Shen, W. Zhang and M. E. Mackay, *Journal of Polymer Sci-*

ence Part B: Polymer Physics, 2014, **52**, 387–396.

22 A. K. Gurnon, P. D. Godfrin, N. J. Wagner, A. P. Eberle, P. Butler and L. Porcar, *J Vis Exp*, 2014, e51068.

23 C. J. Glinka, J. G. Barker, B. Hammouda, S. Krueger, J. J. Moyer and W. J. Orts, *J. Appl. Cryst.*, 1998, **31**, 430–445.

24 S. R. Kline, *Journal of Applied Crystallography*, 2006, **39**, 895–900.

25 P. Kienzle, *Neutron activation and scattering calculator*, Web, 2020, `https://www.ncnr.nist.gov/resources/activation/`.

26 SasView, Web, 2020, `http://www.sasview.org/`.

27 C. Burger, B. S. Hsiao and B. Chu, *Polymer Reviews*, 2010, **50**, 91–111.

28 N. S. Martys, W. L. George, R. P. Murphy and K. M. Weigandt, *Journal of Rheology*, 2020, **64**, 445–457.

29 A. Subbotin, A. Semenov, E. Manias, G. Hadziioannou and G. Tenbrinke, *Macromolecules*, 1995, **28**, 3898–3900.

30 J. T. Padding, E. S. Boek and W. J. Briels, *J Chem Phys*, 2008, **129**, 074903.

31 J. T. Padding, W. J. Briels, M. R. Stukan and E. S. Boek, *Soft Matter*, 2009, **5**, year.

32 R. B. Bird, C. F. Curtiss, R. C. Armstrong and O. Hassager, *Dynamics of Polymer Liquids, Volume 2: Kinetic Theory*, Wiley, New York, 1987.

33 V. K. Natrajan and K. T. Christensen, *Experiments in Fluids*, 2007, **43**, 1–16.

34 R. Lindken, M. Rossi, S. Grosse and J. Westerweel, *Lab Chip*, 2009, **9**, 2551–67.

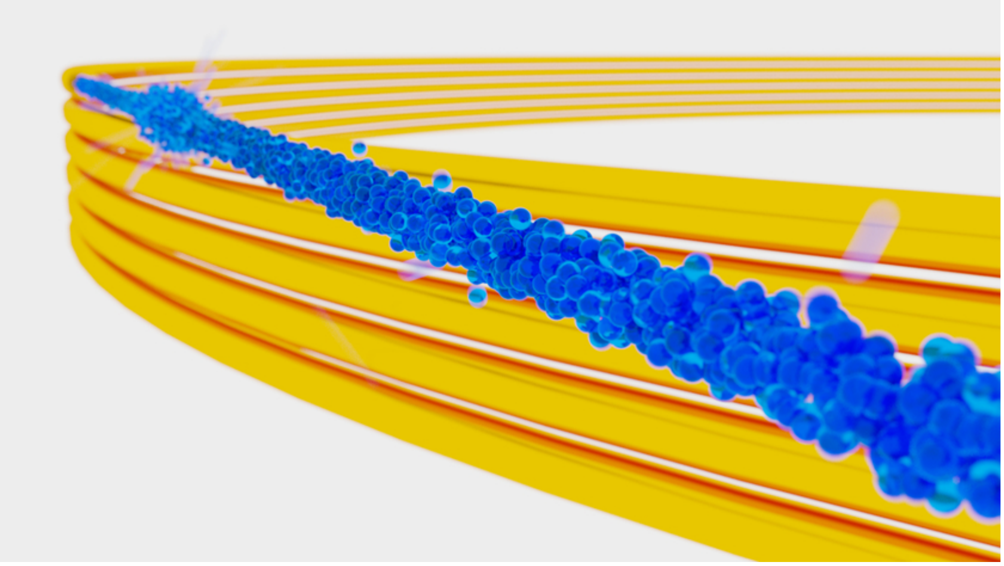

70x39mm (300 x 300 DPI)